ACS APPLIED ENERGY MATERIALS
Cite This: ACS Appl. Energy Mater. 2019, 2, 5427−5437
Article
www.acsaem.org

Stable 6H Organic−Inorganic Hybrid Lead Perovskite and Competitive Formation of 6H and 3C Perovskite Structure with Mixed A Cations

Jiyu Tian,[†] David B. Cordes,[†] Claudio Quarti,*[,‡] David Beljonne,[‡] Alexandra M. Z. Slawin,[†] Eli Zysman-Colman,*[,†,§] and Finlay D. Morrison*[,†]

[†]EaStCHEM School of Chemistry, University of St. Andrews, St. Andrews, Fife KY16 9ST, United Kingdom

[‡]Laboratory for Chemistry of Novel Materials, Department of Chemistry, Université de Mons, Place du Parc 20, 7000 Mons, Belgium

[§]Organic Semiconductor Centre, EaStCHEM School of Chemistry, University of St Andrews, St Andrews, Fife, KY16 9ST, United Kingdom

Supporting Information

ABSTRACT: We report the synthesis and properties of a new organic−inorganic hybrid lead perovskite (OIHP), azetidinium lead bromide ($AzPbBr_3$), possessing the 6H perovskite structure (space group $P6_3/mmc$ with a = 8.745 Å and c = 21.329 Å). This compound has a band gap of 2.81 eV and remains stable for >6 months in the ambient environment. DFT simulations are in fairly good agreement with experiments and indicate that $AzPbBr_3$ is a direct band gap semiconductor. A partial solid solution with the cubic (3C) perovskite methylammonium lead bromide ($Az_{1-x}MA_xPbBr_3$) is possible. In Az-rich 6H compositions the lattice volume and band gap are invariant with x ($\leq$0.3), whereas in the MA-rich 3C phase ($0.8 \leq x \leq 1.0$) the lattice parameters and band gap increase with increasing Az content. Although the relatively large band gap of $AzPbBr_3$ makes it unsuitable for photovoltaic applications, the results indicate Az^+ is a suitable alternative organic A cation for band gap tuning of OHIPs.

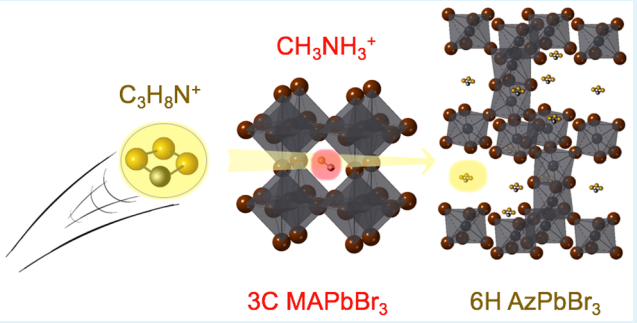

KEYWORDS: *perovskite, organic−inorganic hybrid perovskite, halide perovskite, electronic structure, density functional theory (DFT), dielectric properties*

INTRODUCTION

Organic−inorganic hybrid perovskite (OIHP) materials have emerged as paradigm-shifting materials as their use in solar cells has led to power conversion efficiencies (PCEs) rivalling nanocrystalline silicon solar cells. Since Kojima et al.,[1] who first demonstrated in 2009 the use of methylammonium lead iodide ($MAPbI_3$) as the dye in perovskite solar cells (PSCs), the PCEs of PSCs have steadily increased from 3.8% to 21.6%;[2−6] the same improvement in PCE for Si cells took 20 years to achieve.[7] The use of OIHP materials has since diversified beyond high-efficiency solar cells to photodetectors,[8−10] optically pumped lasers,[11,12] and light-emitting diodes,[13−15] while the photophysical properties underpinning these applications has been thoroughly investigated.[16−18] To illustrate the interest in this field, the number of OHIP-related publications has risen from 34 in 2009 to more than 2400 in 2018,[19] with more than 100000 indexed citations in 2018 alone. OIHPs are currently one of the fastest-growing areas of solid-state/condensed matter science. While much of the understanding of OIHPs borrows from the more mature area of oxide pervoskites, there is still much to learn regarding the solid-state chemistry due to dynamic effects associated with the organic cation molecules, their increased covalency relative to oxides, and also their chemical stability.

OIHPs typically adopt a cubic close-packing perovskite structure of the form ABX_3, where A = an alkylammonium such as methylammonium (MA^+) or formamidinium (FA^+), B = Pb^{2+} or Sn^{2+}, and X = Cl^-, Br^-, or I^-. However, many OIHP compounds are unstable in air as moisture-induced phase changes, which hinders the light-harvesting and electron/hole transportation,[20,21] and this is a detracting feature in their use in photovoltaics. To address the stability issue, different materials design strategies such as mixed cations,[22−24] nanostructuring,[14] and contact passivation[25] have been explored. Density function theory (DFT) calculations predict that the 2H hexagonal (δ-H phase) is more thermodynamically

Received: February 27, 2019
Accepted: July 5, 2019
Published: July 5, 2019

DOI: 10.1021/acsaem.9b00419
ACS Appl. Energy Mater. 2019, 2, 5427−5437

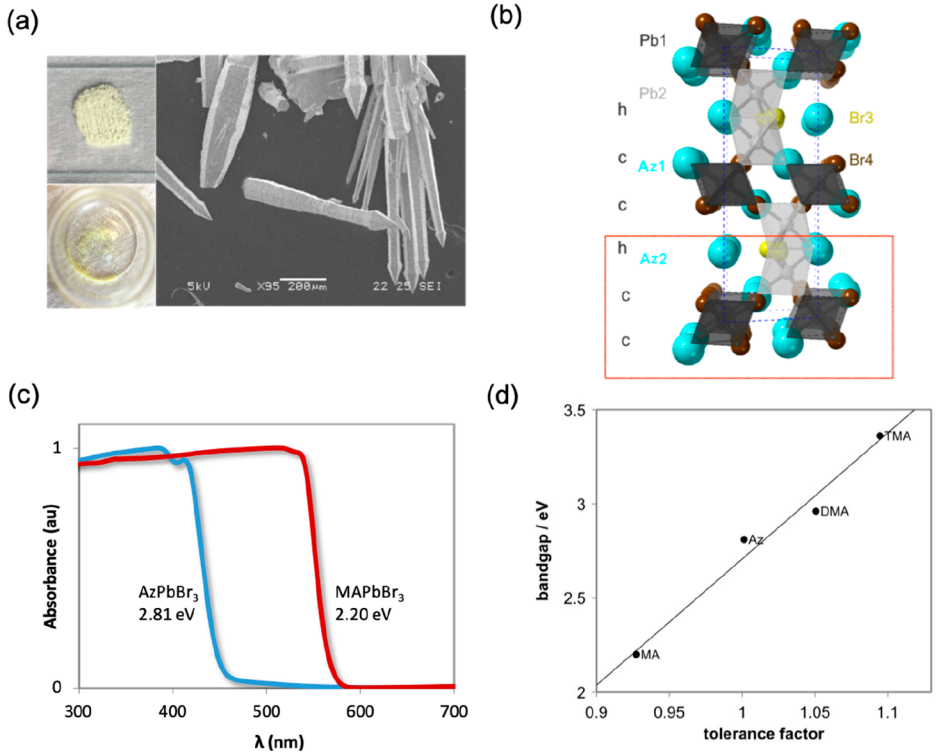

Figure 1. $AzPbBr_3$: (a) optical images of powder and single crystal $AzPbBr_3$ sample (left) and SEM micrograph of single crystals (right); (b) 6H hexagonal perovskite structure as determined from single crystal XRD at 293 K (space group $P6_3/mmc$, lattice parameters a = 8.745 Å and c = 21.329 Å) indicating $(hcc)_2$ packing sequence and combination of face- and corner-sharing octahedra; (c) absorption spectra and associated band gap obtained from $AzPbBr_3$ and $MAPbBr_3$ powders. (d) Dependence of band gap on tolerance factor for lead OIHP with different A cations and resulting close packing of the perovskite structure adopted MA^+(3C), Az^+(6H), DMA^+ (4H), and TMA^+ (2H).[35,36,44]

stable for $APbI_3$ (A = MA and FA);[26,27] this is supported by experimental observations of irreversible color change from black (associated with the cubic phase) to yellow (hexagonal phase) in an ambient environment.[20,28] An alternative possibility to improve long-term stability is to therefore study the formation of the hexagonal phase and slow or prevent the cubic-hexagonal phase transition in the ambient environment. Thus, additional examples of hexagonal perovskite polytypes are needed.

Hexagonal perovskites form a large structural family that consist of only hexagonally (h) close-packed AX_3 layers or sequences of hexagonal (h) and cubic (c) packing; these sequences produce various combinations of face- and corner-sharing octahedra. Because of the change of connectivity of the metal halide octahedra (specifically the B−X−B bond angles in the ABX_3 perovskite), the band gap of the hexagonal perovskite is usually larger than that of cubic perovskite.[29,30] Various nomenclature schemes are used to describe hexagonal perovskites. The most common is Ramsdell notation,[31,32] which takes the form nY, where n denotes the number of stacking layers in the cell and Y indicates the lattice type (R for rhombohedral, H for hexagonal, and C for cubic). Stoumpos et al. found that hexagonal perovskite structures were common in tin-based OIHPs.[33] For lead-based OIHPs, 2H and 4H hexagonal polytypes have been reported with cations such as $NH_2(CH_3)_2^+$(DMA, dimethylammonium) and $NH(CH_3)_3^+$ (TMA, trimethylammonium).[34−37] Gratia et al.[30] also reported a crystallization process with a structural change from 2H, 4H, and 6H (hexagonal) to 3C (cubic) depending on x in the solid solution $(FAPbI_3)_x(MAPbBr_3)_{1-x}$; however, in that study DMSO solvent molecules were found to be present in the crystal lattice, and it is unclear how their presence may affect the exact polymorph adopted as well as its resulting stability.

In this work, we report a new, stable 6H hexagonal lead-based OIHP with $C_3H_6NH_2^+$ (Az, azetidinium) as the A-site cation. Az is a nitrogen-containing four-membered ring.[38,39] The reported hexagonal OIHPs and their tolerance factors are shown in Table S1. The tolerance factor of $AzPbBr_3$ is estimated to be 1.00(1), which is a borderline value for the formation of both cubic and hexagonal structures.[27,40,41] To study the possible transition between 3C and 6H phase, the mixed cation perovskite $MA_xAz_{1-x}PbBr_3$ ($0 < x < 1$) was synthesized, and a complex structure-related change in band gap was observed.

RESULTS AND DISCUSSION

$AzPbBr_3$ Perovskite. The AzBr was synthesized by ion exchange using AzCl and NaBr, and its purity was verified by elemental analysis. The $AzPbBr_3$ material was obtained by mixing stoichiometric dry AzBr with $PbBr_2$ in DMF/DMSO (4:1, by volume); see the Supporting Information for the detailed procedure. Crystals suitable for single crystal X-ray diffraction of $AzPbBr_3$ perovskite were obtained by slow diffusion of the antisolvent chloroform into a solution of perovskite in DMF. $AzPbBr_3$ appears as bright yellow needle-like crystals. SEM micrographs show the crystals to be "spear-like" (Figure 1a and Figure S3) where the hexagonal cross section ranges from 25 to 90 μm and overall length is about 1 mm. Bulk powders appear pale yellow (Figure 1a).

Single crystal XRD (SXRD) at 293 K indicates $AZPbBr_3$ adopts the 6H perovskite structure in the space group $P6_3/mmc$ (Figure 1b). The SXRD data also indicate that the Az

DOI: 10.1021/acsaem.9b00419
ACS Appl. Energy Mater. 2019, 2, 5427−5437

Table 1. Crystallographic Data of the $AzPbBr_3$ Perovskite Obtained from Both Single Crystal and Powder Diffraction Data

	single crystal	single crystal	single crystal[a]	powder (plate)	powder (capillary)	powder (capillary)
T/K	293	173	93	293	293	173
empirical formula	$C_3H_8Br_3NPb$	$C_3H_8Br_3NPb$	$C_3H_8Br_3NPb$	$C_3H_8Br_3NPb$	$C_3H_8Br_3NPb$	$C_3H_8Br_3NPb$
fw	505.02	505.02	505.02			
description	yellow prism	yellow prism	yellow prism	pale yellow	pale yellow	
crystal size/mm^3	0.08 × 0.07 × 0.03	0.09 × 0.06 × 0.02	0.12 × 0.04 × 0.03			
space group	$P6_3/mmc$	$P6_3/mmc$		$P6_3/mmc$	$P6_3/mmc$	$P6_3/mmc$
a/Å	8.745(2)	8.6827(11)	8.608(2)	8.7441(8)	8.746(1)	8.671(7)
c/Å	21.329(4)	21.251(3)	21.345(6)	21.297(1)	21.33(1)	21.23(5)
vol/Å^3	1412.6(7)	1387.5(3)	1369.7(7)	1410.2(3)	1413.1(5)	1382.(9)
Z	6	6				
ρ (calcd)/g/cm^3	3.562	3.626		3.840	3.832	3.916
μ/mm^{-1}	30.634	31.189				
F(000)	1320	1320				
reflns collected	16421	16176		3822	6499	6499
independent reflns (R_{int})	544 (0.0356)	540 (0.0460)				
data/restraints/params	544/0/16	540/0/16				
GOF on F^2	1.176	1.093		9.720[b]	0.8995[b]	0.1860[b]
R_1 [$I > 2\sigma(I)$]	0.0213	0.0233		0.0893[c]	0.0933[c]	0.0688[c]
wR_2 (all data)	0.0559	0.0534		0.1195[d]	0.1240[d]	0.0936[d]
largest diff peak/hole/e/Å^3	0.62, −0.98	0.69, −1.02				

[a]This data is provided as a representative example of obtained data from collections tried at 93 K. Goodness-of-fit parameters for Rietveld refinements of powder data. [b]χ^2. [c]R_p. [d]wR_p; see Figure S6 for refinement profile at 293 K. Note that χ^2 values <1 for the PXRD (capillary) results at 293 and 173 K are due to the poor signal-to-noise of the data obtained (see Figure S7).

cations are situated over high-symmetry lattice sites and showed considerable disorder in early attempts at modeling. As a result they are represented by solid spheres in Figure 1b and are located in the center of electron density associated with the Az cation (see the Supporting Information for details). Rietveld refinement of PXRD data confirms that powder samples adopt the same structure (Table 1). It is interesting to note that despite a similar ionic radius to FA, [r(Az) = 250 pm, r(FA) = 253 pm],[41] $AzPbBr_3$ adopts a hexagonal (6H) perovskite structure in contrast to $FAPbBr_3$ which forms cubic perovskite. The 6H perovskite structure is adopted by the high-temperature hexagonal polymorph of $BaTiO_3$[42,43] and has a $(hcc)_2$ stacking sequence in Jagodzinski notation (i.e., ABCBAC), resulting in pairs of face-sharing octahedra linked by corner-sharing ones. Single crystal and powder crystallographic data are shown in Table 1. Regardless of the synthetic approach (experimental details and PXRD are shown in Table S2 and Figure S4, respectively), $AzPbBr_3$ with the 6H structure was obtained, suggesting that this is the thermodynamically favored phase for this composition. In addition, $AzPbBr_3$ is highly stable in the 6H form and shows no visual or structural degradation when stored in ambient air for at least 6 months (Figure S5).

Optical and Electronic Properties. The absorption spectrum for $AzPbBr_3$ is shown in Figure 1c and is compared to the well-studied 3C perovskite $MAPbBr_3$. The absorption edge for $AzPbBr_3$ is blued-shifted by 122 nm (4920 cm^{-1}, 0.61 eV) and shows a wider band gap, E_g, of 2.81 eV compared to 2.20 eV for $MAPbBr_3$. The increased band gap is consistent with computational predictions that show larger band gaps for face-sharing octahedral systems compared to structures based solely on corner sharing octahedra.[29] Figure 1d shows the dependence of the band gap of OIH lead bromide perovskites as a function of tolerance factor, t, including the present experimental data for $AzPbBr_3$ and $MAPbBr_3$ alongside those reported for 4H hexagonal $DMAPbBr_3$ (experimental data) and 2H hexagonal $TMAPbBr_3$ (calculated).[34,35] As expected, the tolerance factor increases in line with the perovskite polymorph observed (3C < 6H < 4H < 2H), and the increased band gap is consistent with the observations of Stoumpos et al.[33] and Gratia et al.[30] for tin OIHPs and mixed-cation lead OIHPs. The linear trend found for the band gap and tolerance factor (and hence observed polytype) can be attributed to the relative ratio of the cubic close-packing (corner-sharing octahedra) and hexagonal close-packing (face-sharing octahedra) as shown in Table S3. This trend is simply explained by the average B−X−B bond angle, which varies by $(180° - \varphi)$ in ccp perovskites but in mixed h−c systems contains a contribution of ∼90° bonds from the face-sharing octahedra.[45] There is a significant jump in the band gap between 2H and 4H, which may be filled by 9R polytypes that have yet to be reported. From a simple tolerance factor projection, the band gaps of 9R OIHP lead bromide perovskites might be expected to be of the order 3.0−3.2 eV.

To gain a deeper understanding of the electronic properties of the newly synthesized 6H perovskite, we performed periodic density functional theory (DFT) calculations[46] considering the crystalline model obtained from the SXRD. To avoid complications related to the position and orientation of the organic moieties (see Variable Temperature XRD section for discussion), we initially substituted Az with cesium cations. This is a reasonable first approximation for the description of the electronic properties, as the valence and conduction band manifolds in perovskites are dominated by the X and B orbitals,[47] respectively, with the A cation playing little role beyond space filling and charge balance. In performing these calculations, we used fixed lattice parameters at the values obtained from SXRD at 173 K (see Table 1). However, we first performed test calculations to address the role of cell deformations on the electronic properties of the material, finding very small change in the band gap, less than 0.15 eV (see Table S4). We performed calculations adopting the PBE

DOI: 10.1021/acsaem.9b00419
ACS Appl. Energy Mater. 2019, 2, 5427−5437

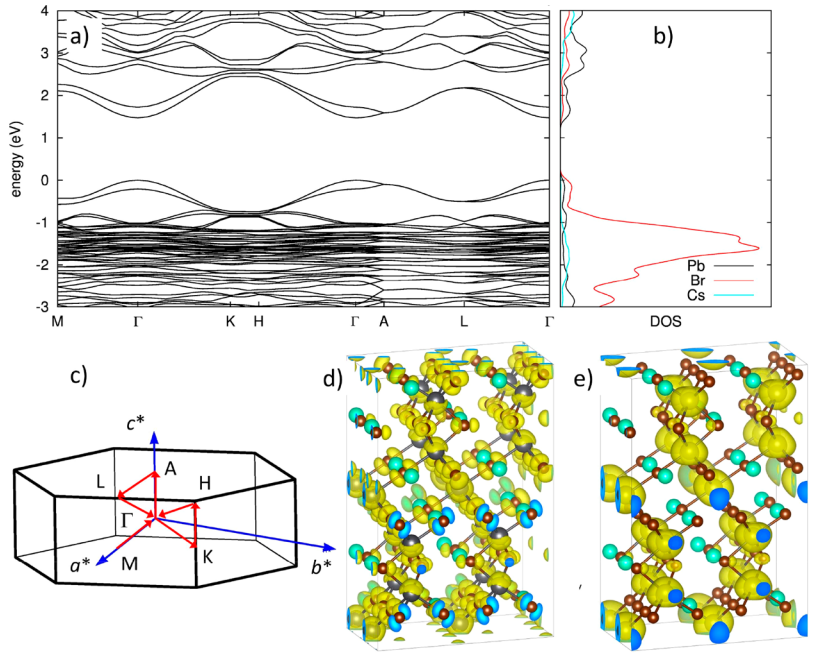

Figure 2. (a) Band structure of 6H "APbBr$_3$" perovskite (calculation with PBE xc-functional, including spin−orbit coupling, A = Cs); the valence band maximum is set to zero. (b) Corresponding partial density of states. (c) First Brillouin zone for hexagonal primitive lattice. (d, e) Wave function localization of the valence band edge (d) and conduction band edge (e) at the Γ point.

exchange-correlation functional,[48] both in the absence of and including spin−orbit coupling, in light of the important role of relativistic effects in dictating the electronic properties of lead-based metal halide perovskites.[49] To clarify how the mixed face-shared/corner-shared octahedral connectivity influences the electronic properties of the present compound, we performed similar DFT calculations on orthorhombic MAPbBr$_3$,[50,51] characterized by purely corner-sharing octahedral packing (Figure S9), again substituting the organic cation with Cs. Notice, however, that the orientation of the organic component was found to affect the general features of the electronic structure only marginally (band gap variations within 0.1−0.2 eV).[52] Details on the adopted computational parameters can be found in the Supporting Information.

The DFT band structure of the 6H "AzPbBr$_3$" perovskite, reported in Figure 2a, clearly indicates that this compound is a direct semiconductor, with both valence and conduction band edges located at the center of the first Brillouin zone. The partial density of states (DOS) of "AzPbBr$_3$" in Figure 2b is qualitatively similar to that of the corner-shared 3C "MAPbBr$_3$" perovskite (Figure S8). Namely, the valence band is principally constituted by 4p orbitals of bromine, with the band edge resulting from the antibonding combination of the 4p atomic orbitals of bromine and 6s orbitals of lead (Figure 2d). Consistently, the conduction band is composed mainly by 6p orbitals from lead, with a small contribution from 4s orbitals of bromine (Figure 2e). Noteworthy, the electronic bands are less dispersed in AzPbBr$_3$ compared to orthorhombic MAPbBr$_3$ (Figure S8). Larger effective masses and consequently decrease of charge carrier mobility are thus anticipated for the mixed face-shared/corner-shared octahedral connectivity, peculiar of 6H perovskites, compared to full corner-shared octahedral connectivity of 3C perovskite.

Neglecting excitonic effects, which are typically very small (∼10^1 meV) for 3C lead halide perovskites,[53,54] the DFT electronic band gap can be compared to the optical band gap from UV−vis measurements in Figure 1c. In this respect, the 0.61 eV blue-shift in the optical absorption from the fully corner-shared, 3C MAPbBr$_3$ structure to the mixed face-shared/corner-shared 6H, AzPbBr$_3$ structure is well reproduced by our DFT calculations (0.47 eV) and even more when spin−orbit coupling is taken into account (0.58 eV, see Figure S8).

We also investigated, more generally, the influence of the organic Az cation on the electronic structure of the AzPbBr$_3$ material, either directly, via specific organic−inorganic interactions, or indirectly, via distortion of the octahedral packing, the latter being a well-known mechanism in 3C perovskite structures.[55] Note that the model adopted here for MAPbBr$_3$, taken as the reference 3C perovskite, is characterized by an in-phase rotation of ∼158° of the octahedra along the *b*-direction,[51] while our SXRD model for the new 6H AzPbBr$_3$ compound presents fully linear bonding for the corner-shared octahedra (no tilting). To address the role of octahedral tilting, we thus performed additional calculations by explicitly introducing Az cations into the structure. Because we were not able to determine the position and orientation of Az cations from XRD measurements (see later discussion), we here adopted three models—two with aligned Az cations (model-1 and model-2, see Figure S9) and one with randomly chosen orientation (model-3)—and performed full atomic relaxation. The resulting relaxed AzPbBr$_3$ structures show tilting of the corner-shared octahedra within the range 162°−178° (see Figure S9). It is interesting to note that these are less distorted, on average, than MAPbBr$_3$. The resulting band gap (computed at the PBE level) varies from 2.56 to 2.65 eV and is hence very close to the one for the untilted Cs-substituted structure (2.55 eV). This further supports our conclusion that the blue-shift of the absorption edge in the UV−vis measurements for AzPbBr$_3$ compared to MAPbBr$_3$ (Figure 1c) is attributed to the change in the organization of the

DOI: 10.1021/acsaem.9b00419
ACS Appl. Energy Mater. 2019, 2, 5427−5437

octahedral linkages, from pure corner-sharing in $MAPbBr_3$ to mixed corner- and face-shared octahedra in $AzPbBr_3$. As a final note, our DFT simulations predict one of the aligned models (model-2) as marginally more stable, but the disordered model-3 lies only 0.01 eV per formula unit higher in energy. This suggests negligible driving force for the cation ordering, with the Az molecules showing small degree of alignment even at low temperature. This could explain the inherent difficulty to resolve the position and orientation of the organic component from XRD measurements, as discussed below.

Dielectric Properties. Electrical characterization of $AzPbBr_3$ using impedance spectroscopy indicated no appreciable conductivity at temperatures up to ca. 200 °C with sample resistivity remaining in excess of 10^7 Ω·cm. Figure 3 shows the

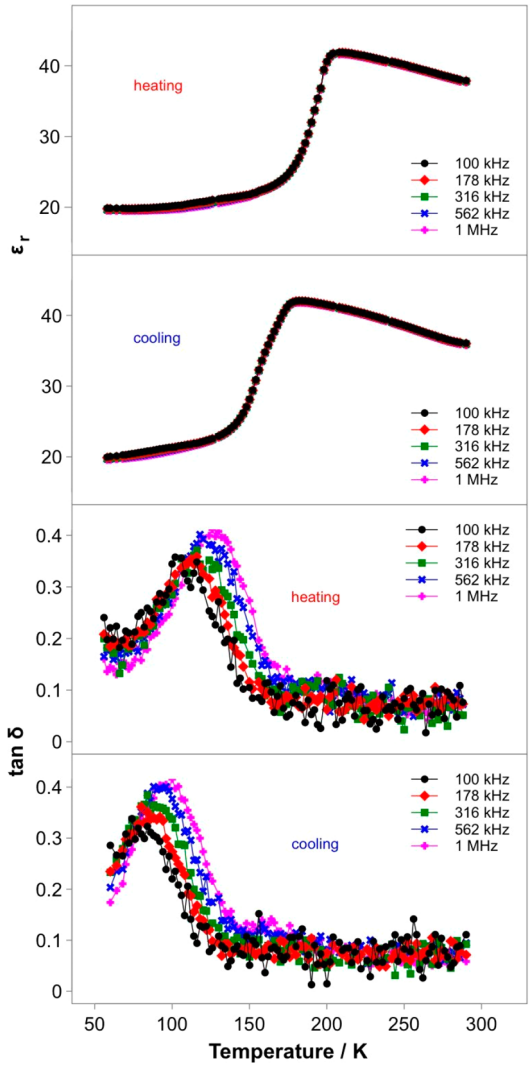

Figure 3. Temperature and frequency dependence of relative permittivity (ε_r) and dielectric loss (tan δ) of $AzPbBr_3$ at a heating/cooling rate of 1 K/min.

dielectric data (relative permittivity, ε_r, and dielectric loss, tan δ) for $AzPbBr_3$ over the temperature range 50−300 K collected on both heating and cooling cycles at 1 K/min. The relative permittivity shows a sharp, frequency-independent peak around 170−190 K on both cooling and heating suggestive of a phase transition. The peak position shows significant thermal hysteresis, which may indicate the transition is first order, but is also likely to have some contribution from thermal lag. The dielectric loss, however, shows a frequency-dependent peak but at slightly lower temperature, ca. 100−120 K, again with some thermal hysteresis. The peak in the permittivity is comparable to that observed in other lead halide OIHPs and is associated with structural phase transitions due to ordering of the A cation.[56] However, as discussed below and previously, both low-temperature XRD data and DFT calculations suggest that this is not the case in this instance. The dielectric loss peak at lower temperature has no clearly associated feature in the permittivity although there is also some evidence of a frequency dependence in ε_r at the corresponding temperature (70−100 K). The large frequency dependence of the loss peak indicates a subtle change in the polarization dynamics, possibly attributable to a change in the Az cation motion, but not static ordering.

Variable-Temperature XRD. Low-temperature XRD measurements were performed on single crystal and powder samples in an attempt to identify the origins of the dielectric anomalies shown in Figure 3. Single crystal data were collected at 293, 173, and 93 K. The 293 and 173 K data show considerable disorder of the Az molecules at the A site with no evidence of a symmetry-breaking phase transition in this range (Table 1).

Data collected at 93 K could be indexed in the primitive trigonal/hexagonal crystal system, with *a* and *c* similar to those seen in the other structures (Table 1), and in good agreement with low-temperature PXRD. However, despite repeated attempts over multiple data collections, neither a unique satisfactory determination of the space group nor refinement of the structure could be made (see the Supporting Information for a more detailed discussion). Several plausible structure solutions could be found in various trigonal or hexagonal space groups, but all refinements attempted for these solutions resulted in significant problems, including multiple nonpositive definite atoms and large numbers of high electron-density peaks, both in proximity to the lead bromide framework and in spaces likely to be occupied by Az^+ cations. This issue is suspected to arise either through the phase transition being incomplete for crystals mounted in the cold stream (despite the crystals being held in the cold stream for extended periods of time) or from a subtle twinning. Attempts were made to determine whether the samples showed twinning in the 93 K data, but no twin laws could be found in any space group tried that resulted in appreciable improvement in data quality. Whatever the nature of the problem in the 93 K SXRD data, it was reversible, as the same crystal could have data recollected at higher temperatures and prove amenable to structure solution.

Although we were unable to determine a unique and satisfactory solution for the low-temperature structure it was possible in most of the plausible solutions in various space groups to locate the lead and bromine atoms. Irrespective of space group, these consistently gave rise to the same 6H Pb−Br framework obtained at higher temperatures, but with some subtle distortions described in detail below. No apparent change in the Az^+ cation behavior was observed at any of the three temperatures; electron density peaks are indicative of these occupying high-symmetry sites in all cases, again consistent with DFT calculations which suggest Az ordering is not favored even at low temperature (Figure S9).

PXRD data collected in 10−20 K increments on cooling from ambient temperature to 88 K are shown in Figure S7.

DOI: 10.1021/acsaem.9b00419
ACS Appl. Energy Mater. 2019, 2, 5427−5437

Visual inspection of the diffraction patterns gave no clear indication of any symmetry breaking: no systematic peak broadening/splitting or additional reflections were observed with decreasing temperature, consistent with the single crystal data. However, the 2D contour plot clearly indicates a change in rate of thermal contraction at around 173 K. Data at all temperatures were refined in the space group $P6_3/mmc$, and the obtained unit cell dimensions as a function of temperature are shown with single crystal data in Figure 4. The data

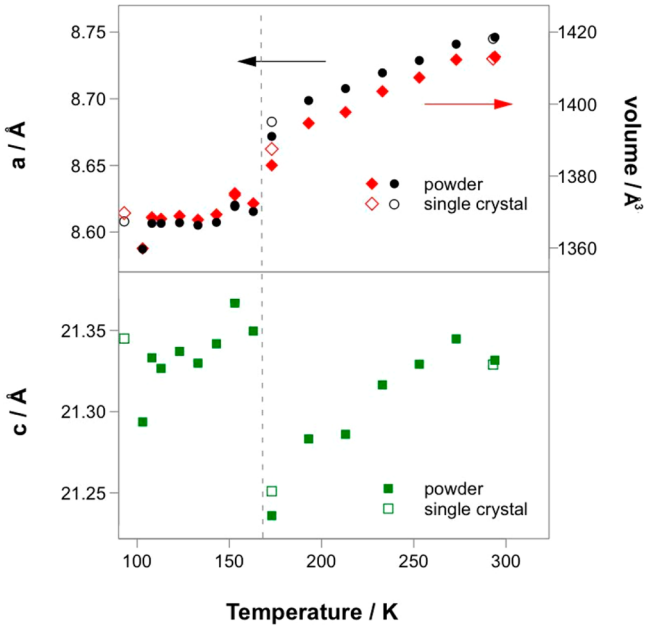

Figure 4. Lattice parameters as a function of temperature for $AzPbBr_3$ obtained from Rietveld refinement of variable temperature PXRD; parameters obtained from SXRD data are also included and are in good agreement.

indicate a clear change on cooling below ca. 173 K where both the *a* parameter and unit cell volume collapse; the *c*-axis also decreases down to 173 K but then expands below this temperature. Note that lattice parameters obtained from SXRD are also in good agreement and confirm this anisotropic behavior. It is also important to highlight that the lattice parameters relatively insensitive to the exact space group used for indexing. Although a unique structural solution was not obtained, it is interesting to examine more generally the nature of the structural behavior at low temperature.

Despite the relative insensitivity of XRD to both the position and dynamics of the light atoms of the Az^+ cation, the Pb−Br positions could be determined with greater certainty (and with little variation with regard to the exact space group used; see the Supporting Information); the behavior of the surrounding Pb−Br framework was therefore studied in more detail to identify possible origins of the anisotropic distortion on cooling below ca. 173 K. Again, in the absence of a unique low-temperature solution, the structural comparisons discussed below are all based on refinements in the $P6_3/mmc$ space group.

The room temperature structure, as determined from the single crystal data, shows some interesting features. For instance, the distances between *c*−*h* and *c*−*c* packing layers are markedly different (Figure 5), resulting in distortion of the octahedra. The elongation of the face-sharing, Pb2-centered octahedra is particularly evident, and the Br−Br packing distance along the *c*-axis is 8% larger compared to that of the corner-sharing Pb1-centered octahedra. This is presumably driven by the Pb−Pb ionic repulsion as the Pb2 atoms are each displaced along the *c*-axis and away from the octahedral barycenter by 0.155 Å. This causes an elongation of the Pb−Br3 bond lengths and reduction in the Pb2−Br3 bond angles to <90°, i.e., those at the point of face-sharing (in the *h*-layer). There is a concomitant compression of the Pb2−Br4 bonds and increase in the Pb2−Br4 bond angles, which form the *c*-

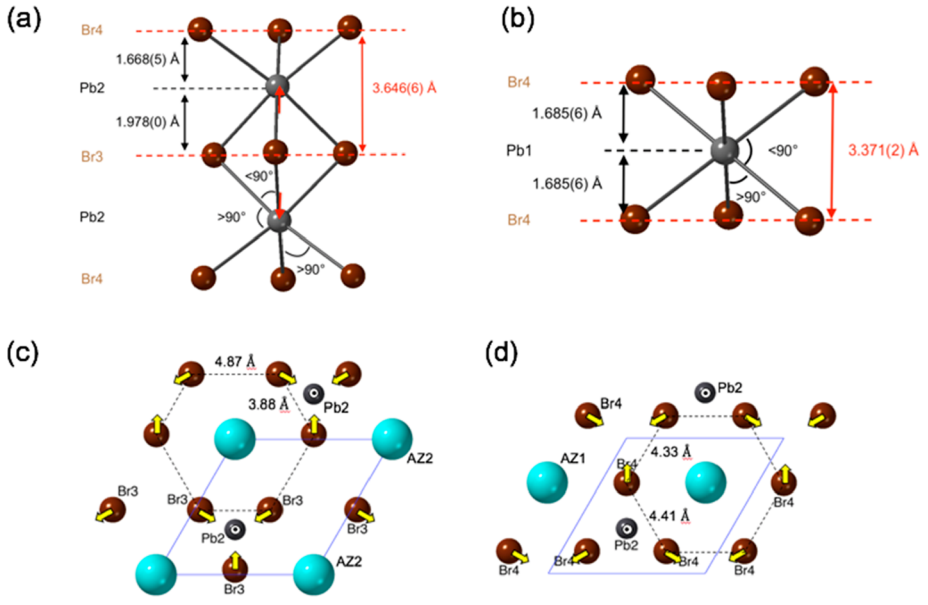

Figure 5. Structural features of 6H $AzPbBr_3$ as determined from single crystal data at 293 K. (a) Face-sharing Pb2 octahedra indicating Pb−Pb repulsion and increased close packing distance compared to Pb1−Br4 octahedra (b) in the *c*-layers; (c) view along *c*-axis showing pinching of Br3 atoms (yellow arrows) which form one face of the Pb2 octahedra in the *h*-layer and (d) concomitant "pushing out" of Br4 atoms in the *c*-layer as the Pb2 atom is displaced along the *c*-axis (in this case, out of the page, as denoted by the circled dot, ⊙).

DOI: 10.1021/acsaem.9b00419
ACS Appl. Energy Mater. 2019, 2, 5427−5437

layers. This is also evident from the short Br3−Br3 (ca. 3.88 Å) and long Br4−Br4 (ca. 4.41 Å) bond lengths that form the opposing faces of the Pb2−Br octahedra in the *ab*-plane (Figure 5c,d). The knock-on effect is that the corner-sharing Pb1 octahedra are uniaxially compressed along the *c*-axis with equivalent Pb1−Br4 bond lengths. Besides the Pb2−Pb2 ionic repulsion, we assume that this distortion is also caused in part by the steric effect of the Pb^{2+} lone pair and also the second order Jahn−Teller effect.[57]

The origin of the anisotropic behavior on cooling is particularly evident from the preliminary structure solutions of both the powder and single crystal diffraction data obtained below 173 K. Initially the crystal undergoes the expected contraction on cooling; however, at 93 K the disparity in the close packing interlayer spacing between *c*−*c* and *c*−*h* layers is dramatically increased (irrespective of space group, Figure S1). From atoms positions determined in $P6_3/mmc$, this arises from a sudden expansion of the *c*−*h* interlayer distance while the *c*−*c* layers continue to contract (Table 2), indicating that the net

Table 2. Variation in Close-Packing Interlayer Distances, Pb2−Pb2 Separation, and Pb2 Off-Centering (Δz) as a Function of Temperature as Determined from Single Crystal XRD Data Refined in $P6_3/mmc$

temp (K)	*c*−*c* distance (Å)	*c*−*h* distance (Å)	Pb2−Pb2 distance (Å)	Δz (Å)
293	3.373	3.646	3.956	0.155
173	3.343	3.641	3.918	0.139
93	3.193	3.740	3.979	0.120

expansion in the *c*-axis on cooling (Figure 4) is driven solely by the *h*−*c* spacing. As a result of this *h*−*c* expansion, although the face-sharing Pb2 octahedra are expanded in the *c*-axis, the Pb2 are less off-centered (Δz = 0.120 Å at 93 K compared to 0.155 Å at 293 K) despite the sudden increase in Pb2−Pb2 separation (Table 2). This suggests the anisotropic behavior and expansion of these octahedra in the *c*-axis is driven by the Pb−Pb repulsion.

In addition to the expansion of the *c*−*h* interlayer spacing there is a significant increase in the distortion of the (Az2, Br3) close packing in the *h*-layer; the pinching of the Br3 atoms which form the shared face of Pb2 octahedra (described for the 293 K structure in Figure 5c) is dramatically increased. The in-plane displacement of the bromide ions in the *h* layer results in a rotation of the shared octahedral face around the *c*-axis. A *cch* stacking portion of the structure is shown at both 293 and 93 K in Figures 6a and 6b, respectively, and clearly reveals the rotation of the shared octahedral face in the *h*-layer at 93 K while the close packing in the *c*-layers and corner-sharing octahedra remain relatively regular. Although we do not have specific information regarding the position or orientation of the Az cations, this distortion in the *h*-layer significantly changes the coordination environment of the Az2 cation. To demonstrate this in more detail, we place an Az2 cation (represented by a sphere for clarity) on the close-packing position with fractional coordinates (0, 0, *z*) where *z* is the same as that of the Br3 anions. The resulting dodecahedral coordination environment for the Az2 cation (Figure 6c) clearly shows that the six in-plane Br3 anions bifurcate further into three alternating short (3.80 Å) and long (4.83 Å) bonds (denoted as Br3 (short) and Br3′ (long); see also Figure S10). The extent of bifurcation is evident by the comparison with the bond distances of 4.52 Å for Az2 to Br4 anions in the adjacent (*c*) layers. As the single crystal data (and DFT calculations) do not appear to suggest any static orientation of the Az cations, this change in environment is unlikely to be driven by hydrogen bonding between Az and Br. Instead, the origin of this distortion is likely due to the Pb2−Pb2 interaction in the face-sharing octahedra.

The degree of octahedral distortion may be determined quantitatively as the octahedral distortion parameter (Δ_1) and bond angle distortion (Δ_2) as defined by[58]

$$\Delta_1 = \frac{1}{6}\sum |R_{av} - R_i|$$

$$\Delta_2 = \frac{1}{12}\sum |90 - \varphi_i|$$

where R_i and φ_i are the respective individual bond lengths and bond angles and R_{av} is the mean Pb−Br bond distance. Distortion indices for $AzPbBr_3$ obtained from single crystal XRD are given in Table 3. Although the (corner-sharing) Pb1 octahedra remain regular in terms of their bonding (Δ_1), indicating that the Pb1 atoms are centered, the octahedra become increasingly compressed in the *c*-axis on cooling, resulting in an increased deviation in the bond angles from 90° (increasing Δ_2). In contrast, the extent of distortion of the face-sharing Pb2 octahedra is relatively consistent at 293 and 173 K with similar values for both Δ_1 and Δ_2 at each

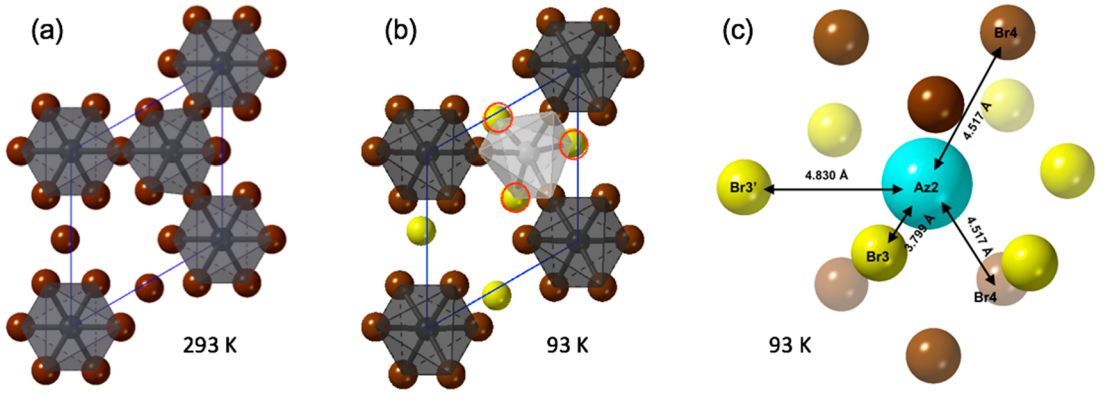

Figure 6. *cch* fragment of the 6H $AzPbBr_3$ structure viewed down the *c*-axis at (a) 293 K and (b) 93 K, highlighting the distortion in the *h* layer (Br3, yellow spheres) at 93 K compared to 293 K. (c) The resulting distortion of the dodecahedral environment occupied by the Az2 cation at 93 K.

DOI: 10.1021/acsaem.9b00419
ACS Appl. Energy Mater. 2019, 2, 5427−5437

Table 3. Octahedral Distortion Parameters for $AzPbBr_3$ Calculated from Single Crystal XRD Data Collected at 293, 173, and 93 K and Refined in $P6_3/mmc$

	293 K		173 K		93 K	
octahedra	Pb1	Pb2	Pb1	Pb2	Pb1	Pb2
Δ_1/Å	0	0.028	0	0.027	0	0.006
Δ_2/deg	1.782	4.369	1.968	4.192	4.204	6.506

temperature. At 93 K, however, we see a clear change: Δ_1 decreases significantly as a result of the more centered Pb2 cations within the octahedra; Δ_2 increases significantly, reflecting the distortion within the *h* (Az, Br3) layer and torsion of the three Br3′ atoms which form the shared face between octahedra.

In the absence of any evidence for loss of Az cation dynamics from variable temperature SXRD (and supported by DFT calculations), the unusual thermal expansion behavior, structural distortion, and large dielectric peak at 173 K are likely driven by a combination of Pb2−Pb2 repulsion and increased steric effect of the Pb lone pair as the thermal motion decreases. The broad, frequency-dependent dielectric loss peak at lower temperature could be due to a change in the Az dynamics. This low unusual low-temperature behavior in $AzPbBr_3$ clearly requires further investigation.

$Az_{1-x}MA_xPbBr_3$ Solid Solution. Although a complete solid solution is not possible due to nonisostructural end members, the degree of replacement of Az by MA in the 6H structure, and similarly replacement of MA by Az in the 3C structure, was investigated by preparing a series of compositions according to $Az_{1-x}MA_xPbBr_3$, $0 \leq x \leq 1$ in 0.1 increments. The resulting powders show a gradual color change from pale yellow in Az-rich compositions to orange with increasing amount of $MAPbBr_3$ (Figure 7a). XRD analysis indicates that for $x \leq 0.3$ only peaks associated with the 6H polymorph are observed and similarly for $x \geq 0.8$ only the 3C phase is present; at intermediate x the XRD indicates a phase mixture of the two phases (Figure 7b).

These results indicate partial solid solutions of both 6H and 3C (Az, MA)$PbBr_3$ phases. The evolution of the PXRD patterns can be observed in Figure S11. The lattice parameters of each polymorph as a function of x were determined by Rietveld refinement, including two phase refinement for intermediate x (the latter show a systematic reduction in the 6H phase fraction with increasing x, Figure S12). The unit cell volume of the 6H phase is invariant as a function of x, Figure 8 (top); presumably, this is due to the incompressibility of the face-sharing Pb2−Br octahedra in the 6H-structure due to the Pb2−Pb2 repulsion, and which does not allow "collapse" of the unit cell volume on insertion of the smaller MA cation. In contrast, the MA-rich 3C solid solution follows Vegard's law and shows a linear increase in unit cell volume with increasing average A cation size. Similar behavior has been observed in the isostructural 6H-3C perovskite oxide solid solution $Ba_{3-x}Sr_xZnSb_2O_9$.[59]

Optical measurements indicate that the absorption edge for the 6H solid solution ($0 \leq x \leq 0.3$) is rather invariant at around 450 nm. By contrast, the 3C solid solution ($0.8 \leq x \leq 1.0$) shows a blue-shift from ca. 560 nm ($x = 1.0$) to ca. 540 nm ($x = 0.8$). In the two-phase region ($0.3 < x < 0.8$) the low volume fraction of 6H phase (Figure S12) means that the absorption is dominated by the 3C component, and the absorption edge remains around 540 nm even for the two-phase mixture at $x = 0.5$. For the $x = 0.4$ composition, which has a significant phase fraction of both 6H and 3C, two

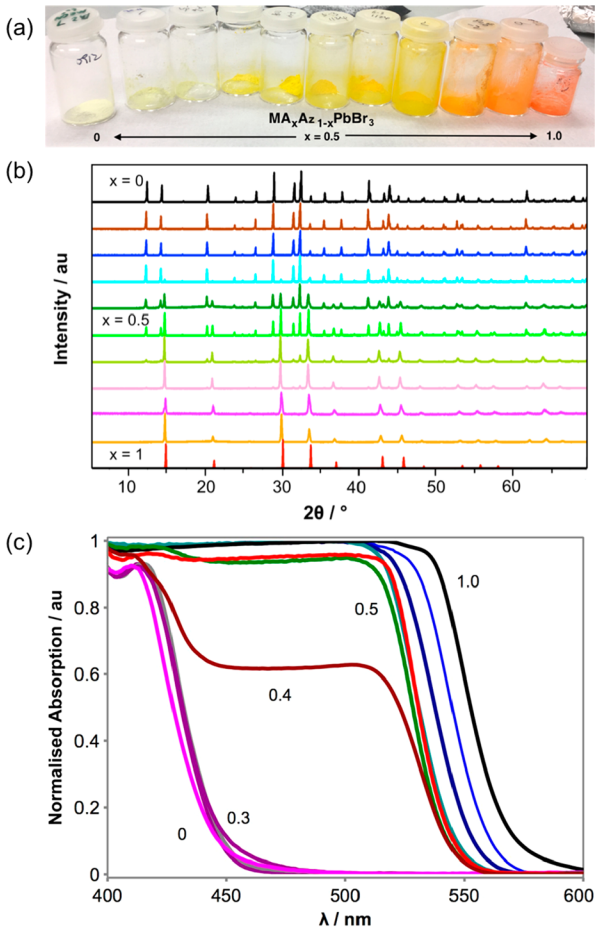

Figure 7. (a) Color change of samples prepared according to composition $Az_{1-x}MA_xPbBr_3$ ($0 \leq x \leq 1$). (b) PXRD data. (c) Absorption spectra as a function of x.

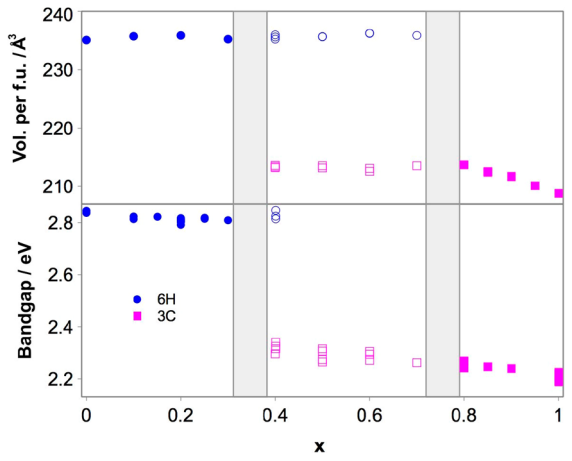

Figure 8. Unit cell volume (expressed per ABX_3 formula unit (f.u.) for ease of comparison) (top) and band gap (bottom) as a function of x for mixed cation compositions $Az_{1-x}MA_xPbBr_3$ ($0 \leq x \leq 1$). Compositions with $0 \leq x \leq 0.3$ and $0.8 \leq x \leq 1.0$ form solid solutions with the 6H and 3C perovskite structures, respectively; a two-phase region forms for intermediate x. The gray regions represent the limits of each solid solution as determined by PXRD. Multiple data points at each value of x represent data for repeated sample syntheses.

DOI: 10.1021/acsaem.9b00419
ACS Appl. Energy Mater. 2019, 2, 5427−5437

absorption edges were observed corresponding to each phase (6H ~ 450 nm; 3C ~ 540 nm). The relative degree of absorption at each wavelength varied from measurement to measurement and sample to sample for this composition, presumably because the measurement is surface-sensitive and depends on the amount of each phase present at the surface during measurement (Figure S13). The band gap values calculated from the onset of the absorption spectra and the crystallographic data as a function of x are self-consistent (Figure 8). The band gap of the 6H phase is relatively independent of x with a value of ~2.8 eV due to the lack of change in unit cell volume and Pb−Br bond lengths, which are reflective of the degree of orbital overlap. For the 3C solid solution the band gap increases slightly with increasing Az content (decreasing x) from ~2.20 eV (x = 0) to ~2.25 eV (x = 0.8), which is consistent with the unit cell expansion as a result of elongation of the Pb−Br bond. Although a limited solid solution is observed for both Az- and MA-rich compositions, a phase transition from cubic to hexagonal and vice versa cannot be induced by merely controlling the A cation ratio. Instead, a region of immiscibility is observed for intermediate x values.

SUMMARY AND CONCLUSIONS

A new OIHP perovskite, azetidinium lead bromide ($AzPbBr_3$), with the 6H perovskite structure has been successfully synthesized. The material is stable in air for >6 months and has an optical band gap of 2.81 eV. DFT calculations are in good agreement with a calculated, direct band gap of 2.55 eV; the larger band gap compared to cubic close-packed (3C) perovskites is predominantly due to poorer connectivity of the Pb−X orbital overlap on introduction of face-sharing octahedra in the hexagonal structure. On cooling $AzPbBr_3$ undergoes a subtle crystallographic distortion but without any identifiable change in space group. This "transition" is evident by an isotropic change in the lattice parameters on cooling (expansion in c and contraction in a) which we propose is driven by the Pb−Pb repulsion in the face-sharing octahedra. Although $AzPbBr_3$ is not suitable for photovoltaic applications due to its large band gap, and the 6H structure is rather resistant to change and band gap tuning through control of A-site cation composition, we demonstrate that Az^+ can partially replace MA^+ in the cubic $MAPbBr_3$ perovskite causing swelling of the lattice and a systematic increase in band gap. This new organic A-site cation (Az) can therefore be used for band gap tuning in alternative OIHP systems.

ASSOCIATED CONTENT

Supporting Information

The Supporting Information is available free of charge on the ACS Publications website at DOI: 10.1021/acsaem.9b00419.

Experimental details, SEM, XRD and absorption spectra data, DFT calculations, and methodology (PDF)

AUTHOR INFORMATION

Corresponding Authors

*E-mail Claudio.QUARTI@umons.ac.be.
*E-mail eli.zysman-colman@st-andrews.ac.uk.
*E-mail finlay.morrison@st-andrews.ac.uk.

ORCID

David B. Cordes: 0000-0002-5366-9168
Claudio Quarti: 0000-0002-5488-1216
David Beljonne: 0000-0002-2989-3557
Eli Zysman-Colman: 0000-0001-7183-6022
Finlay D. Morrison: 0000-0002-2813-3142

Notes

The authors declare no competing financial interest.
The research data supporting this publication can be accessed at https://doi.org/10.17630/344dd782-fb11-4f0b-8cc7-a2190e8c35e.

ACKNOWLEDGMENTS

We thank the Chinese Scholarship Council for Ph.D. Studentship support (to J.T.). We thank Dr. Dianming Sun for his help in running TG analysis. Computational resources have been provided by the Consortium des Équipements de Calcul Intensif (CÉCI), funded by the Fonds de la Recherche Scientifique de Belgique (F.R.S.-FNRS) under Grant 2.5020.11. D.B. is an FNRS Research Director.

REFERENCES

(1) Kojima, A.; Teshima, K.; Shirai, Y.; Miyasaka, T. Organometal Halide Perovskites as Visible-Light Sensitizers for Photovoltaic Cells. *J. Am. Chem. Soc.* **2009**, *131*, 6050−6051.
(2) Yang, W. S.; Park, B.-W.; Jung, E. H.; Jeon, N. J.; Kim, Y. C.; Lee, D. U.; Shin, S. S.; Seo, J.; Kim, E. K.; Noh, J. H.; Seok, S. Il Iodide Management in Formamidinium-Lead-Halide Based Perovskite Layers for Efficient Solar Cells. *Science* **2017**, *356*, 1376−1379.
(3) Mei, A.; Li, X.; Liu, L.; Ku, Z.; Liu, T.; Rong, Y.; Xu, M.; Hu, M.; Chen, J.; Yang, Y.; Gratzel, M.; Han, H. A Hole-Conductor-Free, Fully Printable Mesoscopic Perovskite Solar Cell with High Stability. *Science* **2014**, *345*, 295−298.
(4) Shi, D.; Adinolfi, V.; Comin, R.; Yuan, M.; Alarousu, E.; Buin, A.; Chen, Y.; Hoogland, S.; Rothenberger, A.; Katsiev, K.; Losovyj, Y.; Zhang, X.; Dowben, P. A.; Mohammed, O. F.; Sargent, E. H.; Bakr, O. M. Solar Cells. Low Trap-State Density and Long Carrier Diffusion in Organolead Trihalide Perovskite Single Crystals. *Science* **2015**, *347*, 519−522.
(5) Wang, Z.; Lin, Q.; Chmiel, F. P.; Sakai, N.; Herz, L. M.; Snaith, H. J. Efficient Ambient-Air-Stable Solar Cells with 2D-3D Heterostructured Butylammonium-Caesium-Formamidinium Lead Halide Perovskites. *Nat. Energy* **2017**, *2*, 17135.
(6) Saliba, M.; Matsui, T.; Domanski, K.; Seo, J.-Y.; Ummadisingu, A.; Zakeeruddin, S. M.; Correa-Baena, J.-P.; Tress, W. R.; Abate, A.; Hagfeldt, A.; Grätzel, M. Incorporation of Rubidium Cations into Perovskite Solar Cells Improves Photovoltaic Performance. *Science* **2016**, *354*, 206−209.
(7) https://www.nrel.gov/pv/assets/pdfs/best-reserch-cell-efficiencies.pdf.
(8) Cao, M.; Tian, J.; Cai, Z.; Peng, L.; Yang, L.; Wei, D. Perovskite Heterojunction Based on $CH_3NH_3PbBr_3$ Single Crystal for High-Sensitive Self-Powered Photodetector. *Appl. Phys. Lett.* **2016**, *109*, 233303.
(9) Saidaminov, M. I.; Adinolfi, V.; Comin, R.; Abdelhady, A. L.; Peng, W.; Dursun, I.; Yuan, M.; Hoogland, S.; Sargent, E. H.; Bakr, O. M. Planar-Integrated Single-Crystalline Perovskite Photodetectors. *Nat. Commun.* **2015**, *6*, 8724.
(10) Zhou, H.; Song, Z.; Grice, C. R.; Chen, C.; Yang, X.; Wang, H.; Yan, Y. Pressure-Assisted Annealing Strategy for High-Performance Self-Powered All-Inorganic Perovskite Microcrystal Photodetectors. *J. Phys. Chem. Lett.* **2018**, *9*, 4714−4719.
(11) Zhu, H.; Fu, Y.; Meng, F.; Wu, X.; Gong, Z.; Ding, Q.; Gustafsson, M. V.; Trinh, M. T.; Jin, S.; Zhu, X. Y. Lead Halide Perovskite Nanowire Lasers with Low Lasing Thresholds and High Quality Factors. *Nat. Mater.* **2015**, *14*, 636−642.
(12) Jia, Y.; Kerner, R. A.; Grede, A. J.; Rand, B. P.; Giebink, N. C. Continuous-Wave Lasing in an Organic-Inorganic Lead Halide Perovskite Semiconductor. *Nat. Photonics* **2017**, *11*, 784−788.

DOI: 10.1021/acsaem.9b00419
ACS Appl. Energy Mater. 2019, 2, 5427−5437

(13) Veldhuis, S. A.; Boix, P. P.; Yantara, N.; Li, M.; Sum, T. C.; Mathews, N.; Mhaisalkar, S. G. Perovskite Materials for Light-Emitting Diodes and Lasers. *Adv. Mater.* **2016**, *28*, 6804−6834.
(14) Cho, H.; Jeong, S.-H.; Park, M.-H.; Kim, Y.-H.; Wolf, C.; Lee, C.-L.; Heo, J. H.; Sadhanala, A.; Myoung, N.; Yoo, S.; Im, S. H.; Friend, R. H.; Lee, T.-W. Overcoming the Electroluminescence Efficiency Limitations of Perovskite Light-Emitting Diodes. *Science* **2015**, *350*, 1222−1225.
(15) Zhao, B.; Bai, S.; Kim, V.; Lamboll, R.; Shivanna, R.; Auras, F.; Richter, J. M.; Yang, L.; Dai, L.; Alsari, M.; She, X. J.; Liang, L.; Zhang, J.; Lilliu, S.; Gao, P.; Snaith, H. J.; Wang, J.; Greenham, N. C.; Friend, R. H.; Di, D. High-Efficiency Perovskite-Polymer Bulk Heterostructure Light-Emitting Diodes. *Nat. Photonics* **2018**, *12*, 783−789.
(16) Yang, Z.; Surrente, A.; Galkowski, K.; Bruyant, N.; Maude, D. K.; Haghighirad, A. A.; Snaith, H. J.; Plochocka, P.; Nicholas, R. J. Unraveling the Exciton Binding Energy and the Dielectric Constant in Single-Crystal Methylammonium Lead Triiodide Perovskite. *J. Phys. Chem. Lett.* **2017**, *8*, 1851−1855.
(17) Herz, L. M. Charge-Carrier Mobilities in Metal Halide Perovskites: Fundamental Mechanisms and Limits. *ACS Energy Letters* **2017**, *2*, 1539−1548.
(18) Manser, J. S.; Kamat, P. V. Band Filling with Free Charge Carriers in Organometal Halide Perovskites. *Nat. Photonics* **2014**, *8*, 737−743.
(19) Web of Science. Accessed 20 March 2019. Search Query: (TS = (Hybrid Perovskite OR Perovskite Halide) NOT TS = (Er3* OR Yb3* OR SrT* OR Calcium* OR Maganate* OR Titanate OR Oxi* OR Ceramic)) AND DOCUMENT TYPES: (Article).
(20) Stoumpos, C. C.; Malliakas, C. D.; Kanatzidis, M. G. Semiconducting Tin and Lead Iodide Perovskites with Organic Cations: Phase Transitions, High Mobilities, and near-Infrared Photoluminescent Properties. *Inorg. Chem.* **2013**, *52*, 9019−9038.
(21) Eperon, G. E.; Stranks, S. D.; Menelaou, C.; Johnston, M. B.; Herz, L. M.; Snaith, H. J. Formamidinium of Formamidinium Lead Trihalide: A Broadly Tunable Perovskite for Efficient Planar Heterojunction Solar Cells. *Energy Environ. Sci.* **2014**, *7*, 982.
(22) Pellet, N.; Gao, P.; Gregori, G.; Yang, T. Y.; Nazeeruddin, M. K.; Maier, J.; Grätzel, M. Mixed-Organic-Cation Perovskite Photovoltaics for Enhanced Solar-Light Harvesting. *Angew. Chem., Int. Ed.* **2014**, *53*, 3151−3157.
(23) Jodlowski, A. D.; Roldán-Carmona, C.; Grancini, G.; Salado, M.; Ralaiarisoa, M.; Ahmad, S.; Koch, N.; Camacho, L.; de Miguel, G.; Nazeeruddin, M. K. Large Guanidinium Cation Mixed with Methylammonium in Lead Iodide Perovskites for 19% Efficient Solar Cells. *Nat. Energy* **2017**, *2*, 972−979.
(24) Bi, C.; Chen, B.; Wei, H.; DeLuca, S.; Huang, J. Efficient Flexible Solar Cell Based on Composition-Tailored Hybrid Perovskite. *Adv. Mater.* **2017**, *29*, 1605900.
(25) Tan, H.; Jain, A.; Voznyy, O.; Lan, X.; García de Arquer, F. P.; Fan, J. Z.; Quintero-Bermudez, R.; Yuan, M.; Zhang, B.; Zhao, Y.; Fan, F.; Li, P.; Quan, L. N.; Zhao, Y.; Lu, Z.; Yang, Z.; Hoogland, S.; Sargent, E. H. Efficient and Stable Solution-Processed Planar Perovskite Solar Cells via Contact Passivation. *Science* **2017**, *355*, 722−726.
(26) Thind, A. S.; Huang, X.; Sun, J.; Mishra, R. First-Principles Prediction of a Stable Hexagonal Phase of $CH_3NH_3PbI_3$. *Chem. Mater.* **2017**, *29*, 6003−6011.
(27) Li, Z.; Yang, M.; Park, J. S.; Wei, S. H.; Berry, J. J.; Zhu, K. Stabilizing Perovskite Structures by Tuning Tolerance Factor: Formation of Formamidinium and Cesium Lead Iodide Solid-State Alloys. *Chem. Mater.* **2016**, *28*, 284−292.
(28) Koh, T. M.; Fu, K.; Fang, Y.; Chen, S.; Sum, T. C.; Mathews, N.; Mhaisalkar, S. G.; Boix, P. P.; Baikie, T. Formamidinium-Containing Metal-Halide: An Alternative Material for near-IR Absorption Perovskite Solar Cells. *J. Phys. Chem. C* **2014**, *118*, 16458−16462.
(29) Kamminga, M. E.; De Wijs, G. A.; Havenith, R. W. A.; Blake, G. R.; Palstra, T. T. M. The Role of Connectivity on Electronic Properties of Lead Iodide Perovskite-Derived Compounds. *Inorg. Chem.* **2017**, *56*, 8408−8414.
(30) Gratia, P.; Zimmermann, I.; Schouwink, P.; Yum, J.-H.; Audinot, J.-N.; Sivula, K.; Wirtz, T.; Nazeeruddin, M. K. The Many Faces of Mixed Ion Perovskites: Unraveling and Understanding the Crystallization Process. *ACS Energy Lett.* **2017**, *2*, 2686−2693.
(31) Stein, F.; Palm, M.; Sauthoff, G. Structure and Stability of Laves Phases. Part I. Critical Assessment of Factors Controlling Laves Phase Stability. *Intermetallics* **2004**, *12*, 713−720.
(32) Patrick, L. Inequivalent Sites and Multiple Donor and Acceptor Levels in SiC Polytypes. *Phys. Rev.* **1962**, *127*, 1878−1880.
(33) Stoumpos, C. C.; Mao, L.; Malliakas, C. D.; Kanatzidis, M. G. Structure-Band Gap Relationships in Hexagonal Polytypes and Low-Dimensional Structures of Hybrid Tin Iodide Perovskites. *Inorg. Chem.* **2017**, *56*, 56−73.
(34) Geselle, M.; Fuess, H. Crystal Structure of Dimethylammonium Tribromoplumbate(II), $(CH_3)_2NH_2PbBr_3$. *Z. Kristallogr. Cryst. Struct.* **1997**, *212*, 234−234.
(35) Zaleski, J.; Pietraszko, A. Structure at 200 and 298 K and X-Ray Investigations of the Phase Transition at 242 K of $[NH_2(CH_3)_2]_3Sb_2Cl_9$ (DMACA). *Acta Crystallogr., Sect. B: Struct. Sci.* **1996**, *52*, 287−295.
(36) Mancini, A.; Quadrelli, P.; Amoroso, G.; Milanese, C.; Boiocchi, M.; Sironi, A.; Patrini, M.; Guizzetti, G.; Malavasi, L. Synthesis, Structural and Optical Characterization of $APbX_3$ (A = methylammonium, Dimethylammonium, Trimethylammonium; X = I, Br, Cl) Hybrid Organic-Inorganic Materials. *J. Solid State Chem.* **2016**, *240*, 55−60.
(37) Anelli, C.; Chierotti, M. R.; Bordignon, S.; Quadrelli, P.; Marongiu, D.; Bongiovanni, G.; Malavasi, L. Investigation of Dimethylammonium Solubility in $MAPbBr_3$ Hybrid Perovskite: Synthesis, Crystal Structure, and Optical Properties. *Inorg. Chem.* **2019**, *58*, 944−949.
(38) Pering, S. R.; Deng, W.; Troughton, J. R.; Kubiak, P. S.; Ghosh, D.; Niemann, R. G.; Brivio, F.; Jeffrey, F. E.; Walker, A. B.; Islam, M. S.; Watson, T. M.; Raithby, P. R.; Johnson, A. L.; Lewis, S. E.; Cameron, P. J. Azetidinium Lead Iodide for Perovskite Solar Cells. *J. Mater. Chem. A* **2017**, *5*, 20658−20665.
(39) Zheng, C.; Rubel, O. Aziridinium Lead Iodide: A Stable, Low-Band-Gap Hybrid Halide Perovskite for Photovoltaics. *J. Phys. Chem. Lett.* **2018**, *9*, 874−880.
(40) Becker, M.; Klüner, T.; Wark, M. Formation of Hybrid ABX_3 Perovskite Compounds for Solar Cell Application: First-Principles Calculations of Effective Ionic Radii and Determination of Tolerance Factors. *Dalt. Trans.* **2017**, *46*, 3500−3509.
(41) Kieslich, G.; Sun, S.; Cheetham, T.; Gregor, K.; Shijing, S.; Anthony, K. C. Solid-State Principles Applied to Organic-Inorganic Perovskites: New Tricks for an Old Dog. *Chem. Sci.* **2014**, *5*, 4712−4715.
(42) Akimoto, J.; Gotoh, Y.; Oosawa, Y. Refinement of Hexagonal $BaTiO_3$. *Acta Crystallogr., Sect. C: Cryst. Struct. Commun.* **1994**, *50*, 160−161.
(43) Sinclair, D. C.; Skakle, J. M. S.; Morrison, F. D.; Smith, R. I.; Beales, T. P. Structure and Electrical Properties of Oxygen-Deficient Hexagonal $BaTiO_3$. *J. Mater. Chem.* **1999**, *9*, 1327−1331.
(44) Geselle, M.; Fuess, H. Crystal Structure of Tetrakis-(Ethylammonium) Decachlorotriplumbate(II), $(C_2H_5NH_3)_4Pb_3Cl_{10}$. *Z. Kristallogr. - New Cryst. Struct.* **1997**, *212*, 241−242.
(45) Goodenough, J. B.; Zhou, J.-S. Localized to Itinerant Electronic Transitions in Transition-Metal Oxides with the Perovskite Structure. *Chem. Mater.* **1998**, *10*, 2980−2993.
(46) Giannozzi, P.; Baroni, S.; Bonini, N.; Calandra, M.; Car, R.; Cavazzoni, C.; Ceresoli, D.; Chiarotti, G. L.; Cococcioni, M.; Dabo, I.; Dal Corso, A.; de Gironcoli, S.; Fabris, S.; Fratesi, G.; Gebauer, R.; Gerstmann, U.; Gougoussis, C.; Kokalj, A.; Lazzeri, M.; Martin-Samos, L.; Marzari, N.; Mauri, F.; Mazzarello, R.; Paolini, S.; Pasquarello, A.; Paulatto, L.; Sbraccia, C.; Scandolo, S.; Sclauzero, G.; Seitsonen, A. P.; Smogunov, A.; Umari, P.; Wentzcovitch, R. M. QUANTUM ESPRESSO: A Modular and Open-Source Software

DOI: 10.1021/acsaem.9b00419
ACS Appl. Energy Mater. 2019, 2, 5427−5437

Project for Quantum Simulations of Materials. *J. Phys.: Condens. Matter* **2009**, *21*, 395502.
(47) Goodenough, J. B. Metallic Oxides. *Prog. Solid State Chem.* **1971**, *5*, 145−399.
(48) Perdew, J. P.; Burke, K.; Ernzerhof, M. Generalized Gradient Approximation Made Simple. *Phys. Rev. Lett.* **1996**, *77*, 3865−3868.
(49) Even, J.; Pedesseau, L.; Jancu, J.-M.; Katan, C. Importance of Spin-Orbit Coupling in Hybrid Organic/Inorganic Perovskites for Photovoltaic Applications. *J. Phys. Chem. Lett.* **2013**, *4*, 2999−3005.
(50) Poglitsch, A.; Weber, D. Dynamic Disorder in Methylammoniumtrihalogenoplumbates (II) Observed by Millimeter-Wave Spectroscopy. *J. Chem. Phys.* **1987**, *87*, 6373.
(51) Mashiyama, H.; Kawamura, Y.; Kubota, Y. The Anti-Polar Structure of $CH_3NH_3PbBr_3$. *J. Korean Phys. Soc.* **2007**, *51*, 850−853.
(52) Quarti, C.; Mosconi, E.; De Angelis, F. Interplay of Orientational Order and Electronic Structure in Methylammonium Lead Iodide: Implications for Solar Cell Operation. *Chem. Mater.* **2014**, *26*, 6557−6569.
(53) D'Innocenzo, V.; Grancini, G.; Alcocer, M. J. P.; Kandada, A. R. S.; Stranks, S. D.; Lee, M. M.; Lanzani, G.; Snaith, H. J.; Petrozza, A. Excitons versus Free Charges in Organo-Lead Tri-Halide Perovskites. *Nat. Commun.* **2014**, *5*, 3586.
(54) Miyata, A.; Mitioglu, A.; Plochocka, P.; Portugall, O.; Wang, J. T.-W.; Stranks, S. D.; Snaith, H. J.; Nicholas, R. J. Direct Measurement of the Exciton Binding Energy and Effective Masses for Charge Carriers in Organic-Inorganic Tri-Halide Perovskites. *Nat. Phys.* **2015**, *11*, 582−587.
(55) Amat, A.; Mosconi, E.; Ronca, E.; Quarti, C.; Umari, P.; Nazeeruddin, M. K.; Grätzel, M.; De Angelis, F. Cation-Induced Band-Gap Tuning in Organohalide Perovskites: Interplay of Spin-Orbit Coupling and Octahedra Tilting. *Nano Lett.* **2014**, *14*, 3608−3616.
(56) Maeda, M.; Hattori, M.; Hotta, A.; Suzuki, I. Dielectric Studies on $CH_3NH_3PbX_3$ (X = Cl and Br) Single Cystals. *J. Phys. Soc. Jpn.* **1997**, *66*, 1508−1511.
(57) Bersuker, I. B. Critical Review of Contributions to the Jahn-Teller Symposium JT2010 and Beyond. In *Vibronic Interactions and the Jahn-Teller Effect: Theory and Applications*; Atanasov, M., Daul, C., Tregenna-Piggott, P. L. W., Eds.; Springer Netherlands: Dordrecht, 2012; pp 1−22.
(58) Cordrey, K. J.; Stanczyk, M.; Dixon, C. A. L.; Knight, K. S.; Gardner, J.; Morrison, F. D.; Lightfoot, P. Structural and Dielectric Studies of the Phase Behaviour of the Topological Ferroelectric $La_{1-x}Nd_xTaO_4$. *Dalt. Trans.* **2015**, *44*, 10673−10680.
(59) Li, J.; Jiang, P.; Gao, W.; Cong, R.; Yang, T. Chemical Substitution-Induced and Competitive Formation of 6H and 3C Perovskite Structures in $Ba_{3-x}Sr_xZnSb_2O_9$: The Coexistence of Two Perovskites in $0.3 \leq x \leq 1.0$. *Inorg. Chem.* **2017**, *56*, 14335−14344.

DOI: 10.1021/acsaem.9b00419
ACS Appl. Energy Mater. 2019, 2, 5427−5437